Direct Observation of Interfacial Morphology in Poly(3-hexylthiophene) Transistors: Relationship between Grain Boundary and Field-Effect Mobility

Danbi Choi,[†,‡] Sangwoo Jin,[†,§] Youngmin Lee,[⊥] Se Hyun Kim,[‡] Dae Sung Chung,[‡] Kipyo Hong,[‡] Chanwoo Yang,[‡] Jungwoon Jung,[§] Jin Kon Kim,[⊥] Moonhor Ree,*,[§] and Chan Eon Park*,[‡]

Polymer Research Institute, Department of Chemical Engineering, Pohang University of Science and Technology, Pohang, 790-784, Korea, Department of Chemistry, National Research Lab for Polymer Synthesis & Physics, Pohang Accelerator Laboratory, Center for Electro-Photo Behaviors in Advanced Molecular Systems, Division of Advanced Materials Science, Polymer Research Institute, BK School of Molecular Science, and Pohang University of Science and Technology, Pohang, 790-794, Korea, and National Creative Research Initiative Center for Block Copolymer Self-Assembly, Department of Chemical Engineering and Polymer Research Institute, Pohang University of Science and Technology, Kyungbuk 790-784, Republic of Korea

ABSTRACT We investigated the effects of microstructural (crystallization and molecular orientation) and morphological alternation (grain boundary) of poly(3-hexylthiophene) (P3HT) films on the field-effect mobility (μ) before (as-spun P3HT) and after (melt-crystallized P3HT) melting of P3HT films. Although grazing incidence X-ray scattering shows that melt-crystallized P3HT has a more highly ordered edge-on structure than as-spun P3HT, the melt-crystallized P3HT reveals $\mu = 0.003$ cm^2 V^{-1} s^{-1}; this is an order of magnitude lower than that of as-spun P3HT ($\mu = 0.01$ cm^2 V^{-1} s^{-1}). In addition, the interfacial morphologies of the bottom surfaces of P3HT films, which are attached to the gate dielectric, were investigated using a film transfer technique. The melt-crystallized P3HT at this interface consists of well-developed nanowire crystallites with well-defined grain boundaries that act as trap states, as verified by analysis of the temperature-dependence of μ. The remarkable reduction of μ in low-molecular-weight P3HT film (8 kg/mol) that results from melt-crystallization is due to the increased number of well-defined grain boundaries.

KEYWORDS: P3HT • melt-crystallization • interfacial morphology • field-effect mobility • grain boundary

INTRODUCTION

Conjugated polymeric semiconductors are potential components of next-generation large-area flexible electronic technologies (1). Recent research has focused on solution-processed organic thin film transistors (OTFTs), which show good device performance (e.g., high field-effect mobility, low threshold voltage, low subthreshold swing, and high current on/off ratio) (2, 3). However, to achieve device performances comparable to those of amorphous silicon transistors, and to fully realize the low-cost aspects of OTFTs, we must develop methods that can produce semiconducting layers by solution-processing techniques such as spin-casting or inkjet printing. For this reason, poly(3-hexylthiophene) (P3HT) has been investigated because it has good solubility in various organic solvents and also has self-assembly characteristics (4−6). Despite these merits, P3HT does not have noticeably high field-effect mobility (μ) due to poor crystallinity and poor molecular orientation. To overcome these drawbacks, several research groups have tried modifying P3HT using thermal annealing. Some have reported that this process generally improved the crystallinity of P3HT film and enhanced μ (7−12), possibly because microstructurally arranged P3HT film with expanded crystallites enhanced hole conduction (7). However, several groups reported decreased μ after thermal annealing of P3HT film; suggested explanations for this decrease include morphological decomposition of the P3HT films at temperatures >150 °C (10) and temperature-induced transformations in conjugation length of P3HT chains (11).

Because thermal annealing simultaneously alters the crystallinity and morphology of P3HT film (10), the effect of annealing temperature on microstructures and morphologies of P3HT films should be determined. Particularly, the
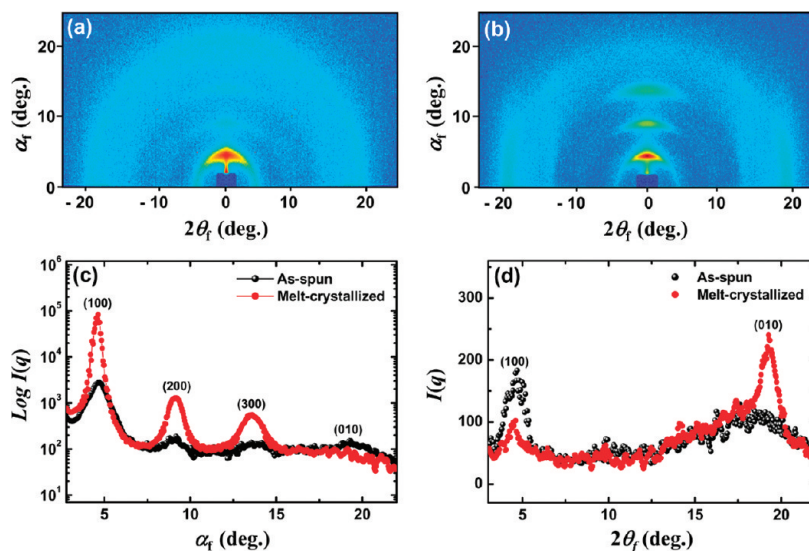
FIGURE 1. 2D GIXS patterns measured at $\alpha_i = 0.18°$ for (a) as-spun and (b) melt-crystallized films. 1D GIXS profiles extracted from 2D GIXS patterns in the α_f direction (c) at $2\theta_f = 0°$ and in the $2\theta_f$ direction (d) at $\alpha_f = 0.18°$.

interfacial microstructures and morphologies of P3HT film near the gate dielectric should be studied, because holes flow in a conducting channel formed at the interface between the gate dielectric and the semiconductor.

In this paper, we investigate P3HT films before (as-spun P3HT) and after (melt-crystallized P3HT) melting to determine how μ is affected by the microstructure and morphology of films at the interface between the gate dielectric and the semiconductor layer. We used the film transfer technique to directly observe the interfacial morphologies of films of P3HT and investigated how charge transport depends on the microstructural and the morphological changes in P3HT layers. We determined that to realize P3HT-based OTFTs with high μ, control of interfacial morphology of the P3HT layer is as important as improvement of its structure.

EXPERIMENTAL SECTION

Materials. Three different P3HTs with different molecular weights were used. High-molecular-weight regioregular (RR) P3HT (P3HT, 26 kg/mol M_n (number-average molecular weight), 1.69 PDI (polydispersity index)) and RR P3HT electronic grade (P3HT-20, $\bar{M}_n = 20$ kg/mol, PDI = 1.77), both purchased from Aldrich, were purified by Soxhlet extraction before use. Low-molecular-weight P3HT was synthesized as described earlier (13). After polymerization, P3HT was first isolated by methanol precipitation, then purified by Soxhlet extraction with methanol and hexane. In the remaining P3HT, low-molecular-weight P3HT was fractionated with dichloromethane by Soxhlet extraction. (P3HT-8, $\bar{M}_n = 8$ kg/mol, PDI = 1.43) The regioregularity (92%) was determined from the integration ratio of relevant peaks (approximately 2.8 ppm) in the ^{1}H NMR spectrum.

Preparation of the Devices. A heavily doped (100) Si wafer was used as the gate electrode and a thermally grown 300-nm-thick layer of SiO_2 was used as the gate dielectric. Before the deposition of Au, the gate dielectric surface was modified using octadecyltrichlorosilane (ODTS) or hexamethyldisilazane (HMDS) to convert the surface from hydrophilic to hydrophobic. Source and drain electrodes were then defined on the gate dielectric using a shadow mask. Finally, P3HT was spin-coated at 2000 rpm for 60 s; the resulting film was approximately 100−110 nm thick.

After spin coating, two different P3HT transistors were prepared. The as-spun transistor was dried in a desiccator for a day without heat treatment. The P3HT on the melt-crystallized transistor was melted at 240 °C for 10 min and recrystallized by cooling it to room temperature in a vacuum oven.

Characterization. Grazing incident X-ray scattering (GIXS) measurements were conducted at the 4C2 beamline in the Pohang Accelerator Laboratory using a monochromatized X-ray radiation source of 8.979 eV ($\lambda = 0.138$ nm) and a two-dimensional (2D) charge-coupled device (CCD) detector (Roper Scientific, Trenton, NJ) (14−16). The sample-to-detector distance was 132.7 mm. The samples were mounted on a home-made z-axis goniometer equipped with a vacuum chamber. The incidence angle (α_i) of each X-ray beam was set in the range 0.18−0.20°. Scattering angles were determined from the positions of X-ray beams reflected from the silicon substrate interface for various α_i by using precalibrated silver behenate (TCI, Japan). Data were typically collected for 3 s.

Specular X-ray reflectivity (SXR) measurements were conducted at the 3C2 beamline in the Pohang Accelerator Laboratory (17). The samples were mounted on a HUBER four-circle goniometer, and a scintillation counter with an enhanced dynamic range (Bede Scientific, EDR) was used as a detector. The horizontal beam size at the sample position was ca. 2 mm, and the full width at half-maximum of the direct beam profile measured by a detector scan was 0.015°. The measured reflected intensities were normalized to the intensity of the incident beam, which was monitored using an ionization chamber.

The morphologies of the top and bottom surfaces of the P3HT layers were investigated using atomic force microscopy (AFM; Digital Instrument Multimode SPM) in tapping mode. The electrical characteristics of the P3HT OTFTs were determined using Keithley 2400 and 236 source/measure units under a N_2 atmosphere to prevent penetration of oxygen and water from the atmosphere. The change in μ between 180 K and room temperature was measured using a cryostat system, and the activation energy for charge transport was extracted from these measurements.

RESULTS AND DISCUSSION

Two-dimensional GIXS patterns and their one-dimensional (1D) profiles were obtained for the as-spun and the melt-crystallized P3HT films (Figure 1) (18, 19). The 1D profile of the as-spun film had an intense (100) peak with weak high order peaks along the α_f direction. A (100) peak and a broad isotropic peak were indentified in the $2\theta_f$
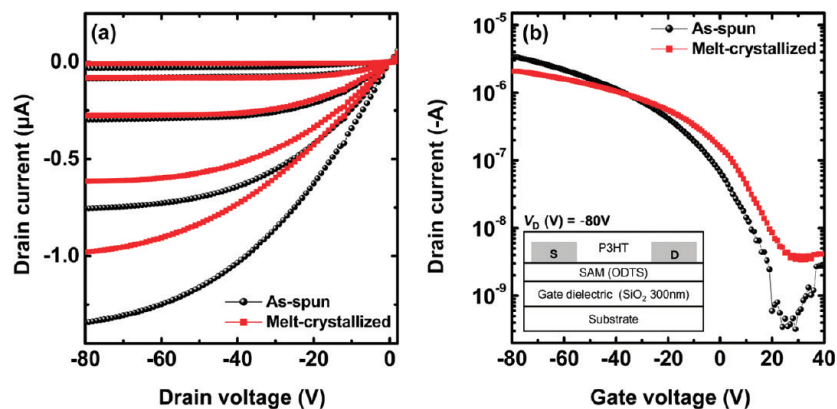
FIGURE 2. (a) I_D-V_D output characteristics for high-molecular-weight P3HT (26 kg/mol) OTFTs fabricated with (melt-crystallized) and without (as-spun) thermal treatment. (b) I_D-V_G transfer characteristics in the saturation regime ($V_D = -80$ V). All measurements were made under N_2 conditions. The inset shows schematic structure of bottom contact P3HT OFETs.

direction. These scattering features reveal that the P3HT molecules have mixed edge-on and face-on orientations on the substrate. In addition, the broad and weak high order peaks indicate that the as-spun P3HT film has poor crystallinity and poor orientation (1, 20−22). In contrast, the 1D scattering profile of the melt-crystallized P3HT film exhibits considerably increased crystallinity with strong high order peaks along the α_f direction. The melting and recrystallization of the hydrophobic surface caused a change in the edge-on orientation: the scattering patterns in the $2\theta_f$ direction are entirely complementary in the melt-crystallized P3HT films compared to the as-spun films; the (100) peak (face-on orientation) is smaller, whereas the (010) peak due to $\pi-\pi$ interchain stacking (edge-on orientation) is increased. These structural changes in preferred orientation enable holes to move in the conjugation direction, and result in high μ. In summary, both crystallinity and molecular orientation of the melt-crystallized P3HT film change to a form that should allow better device performance.

The characteristics of the as-spun and the melt-crystallized P3HT OTFTs were measured in an N_2 environment (Figure 2). The output curves show that these devices exhibit good linear/saturation behavior. Drain voltages were swept from 2 to −80 V at different gate biases of 0, −20, −40, −60, and −80 V (Figure 2a). The values of μ were extracted from plots of the square root of the drain-source current I_{DS} versus gate voltage (V_G) in the saturation regime ($V_{DS} = -80$ V) as: $I_{DS} = (WC_i/2L)\mu(V_G - V_{th})^2$ (Figure 2b), where W is channel width, C_i is the capacitance per unit area of the gate dielectrics, L is channel length, and V_{th} is threshold voltage. Although melt-crystallized P3HT has better crystallinity and better $\pi-\pi$ stacked orientation in the charge transport direction than does as-spun P3HT, $\mu = 3 \times 10^{-3}$ cm^2 V^{-1} s^{-1} in the melt-crystallized P3HT; this value is an order of magnitude lower than that in the as-spun P3HT ($\mu = 1 \times 10^{-2}$ cm^{2}V^{-1}s^{-1}). Moreover, the on/off current ratio of the melt-crystallized P3HT device is more than an order of magnitude (6.14×10^2) lower than that in the as-spun device (1.04×10^4).

Because the melt-crystallized P3HT had better crystallinity but inferior μ and on/off current ratio than as-spun P3HT, the interfacial morphology between the gate dielectric and
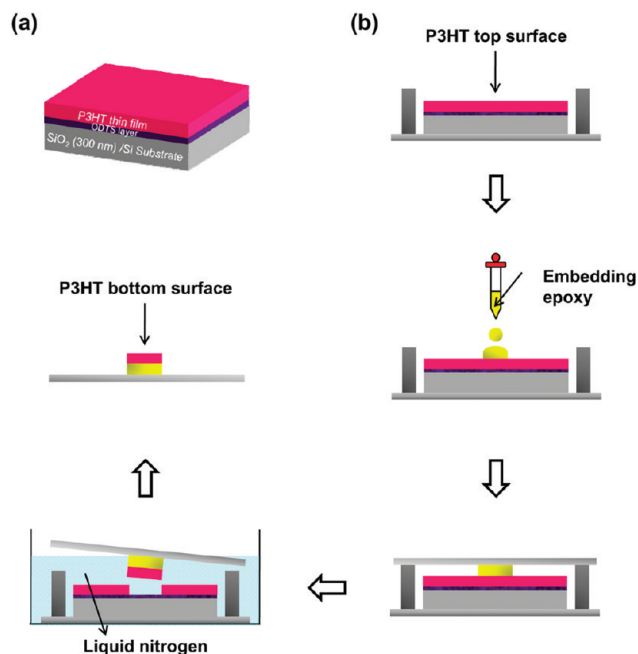

FIGURE 3. (a) Structure of P3HT and ODTS-treated SiO$_2$; (b) schematic diagram of the fabrication process in the film transfer technique, which embeds epoxy on the P3HT surface.

the semiconductor within 5 nm of the semiconductor layers were investigated to determine the cause of the poor performance of the melt-crystallized P3HT. Films of the bottom of the P3HT were obtained using the film transfer technique (Figure 3): the P3HT film was spin-coated onto an ODTS-treated SiO$_2$ substrate, then an embedding epoxy (Polybed 812 Kit) was dropped onto the top surface of the P3HT film and cured under ambient conditions for one day. The epoxy-P3HT complex was peeled off by immersing it in liquid nitrogen. The detached width of P3HT was 7 mm on average (see the Supporting Information, Figure S1). From the X-ray photoelectron spectroscopy of peeled specimens, we see that detached P3HT films exhibit only a sulfur-based peak, whereas their counterparts exhibit only silicon peaks from silicon wafer and SiO$_2$, implying that the P3HT film is completely detached from the SiO$_2$ substrate (see the Supporting Information, Figure S2).
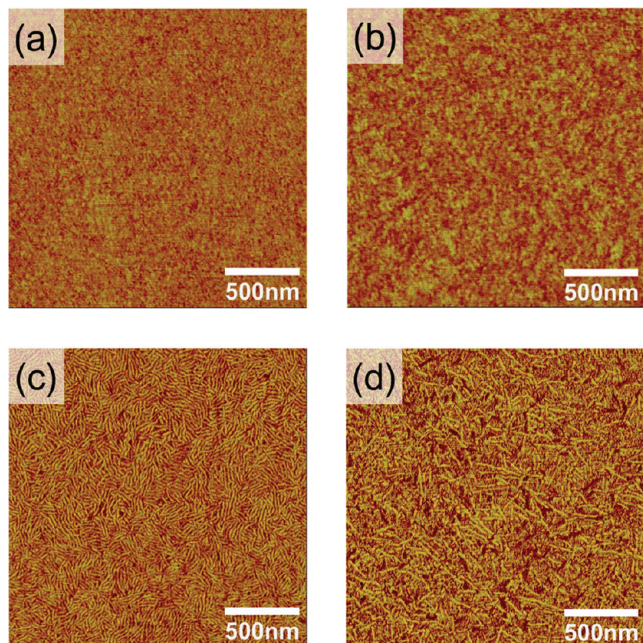
FIGURE 4. Phase images of the top and bottom surfaces of P3HT films (26 kg/mol) obtained with tapping mode atomic force microscopy: (a) top surface of as-spun P3HT, (b) bottom surface of as-spun P3HT, (c) top surface of melt-crystallized P3HT, (d) bottom surface of melt-crystallized P3HT.

The top surface of the as-spun film showed an isotropic nodulelike morphology (Figure 4a). In contrast, the top surface of melt-crystallized film showed well-developed nanowirelike crystallites (Figure 4c). These differences in surface morphology are closely related to intermolecular rod-to-rod association (23). The bottom morphologies of the as-spun and the melt-crystallized films were similar to their own top morphologies, but very different from each other. The as-spun film showed continuously connected uniform morphology throughout the entire area, whereas the melt-

crystallized film contained numerous voids and confined grain boundaries between well-developed crystallites (Figure 4d). This characteristic implies that the holes flowing inside each crystal are slowed by the need to hop the gaps between crystallites, so that such grain-boundary-limited charge transport causes decrease in μ. Several papers have attributed the poor mobility of low-molecular-weight P3HT to a highly ordered crystalline structure with well-defined grain boundaries (24−26). In sexi-thiophene the resistance is significantly higher across the grain boundary than within grains; this observation suggests that the grain boundary forms a high-energy barrier to charge transfer (27).

Structural and morphological properties of interfaces in the as-spun and the melt-crystallized P3HT films were studied using SXR (Figure 5), which provides information about film thickness, roughness of free space and interface, and the electron density of the film (17). The profiles clearly show the critical angles of the film ($\alpha_{c,f}$) and the substrate ($\alpha_{c,s}$) over q_z range $0.2 - 0.35$ nm^{-1}; here, q_z is the magnitude of the scattering vector along the direction of the film thickness. Oscillations between $\alpha_{c,f}$ and $\alpha_{c,s}$ are also clearly discernible; these are due to waveguide modes of the X-ray beam confined in the film. Thus reflected intensity is close to the incident intensity, although slightly lower because of a certain degree of X-ray beam absorption in the film. The steeply decaying reflectivity curve is modulated by high-frequency oscillations (Kiessig fringes), which are due to the interference between the X-ray beams reflected from air/film and the film/substrate interfaces (17). The features almost disappeared after melt-crystallization (Figure 5b), indicating the roughnesses of air/film surface and film/substrate interface much increased through the melt-crystallization.

Structural parameters from the SXR data were quantitatively calculated using the Parratt formalism (Table 1). All
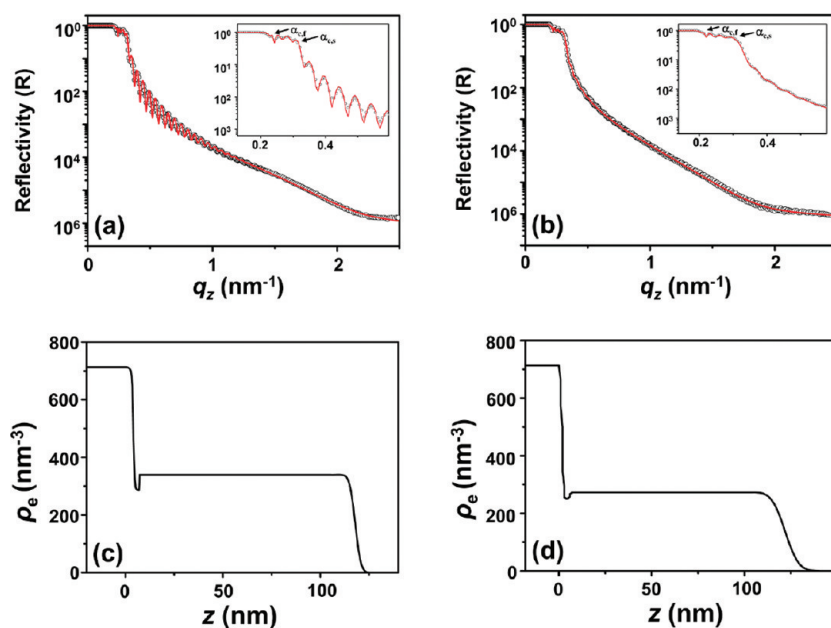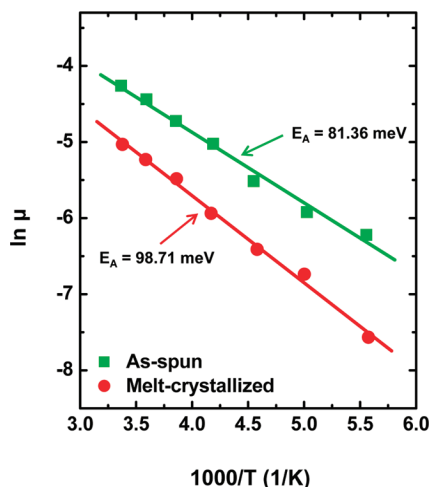

FIGURE 5. Specular X-ray reflectivity profiles of (a) as-spun and (b) melt-crystallized P3HT films, and fitted electron density of (c) as-spun and (d) melt-crystallized P3HT films.

Table 1. Structural Parameters of As-Spun and Melt-Crystallized P3HT Films Calculated by SXR Using the Parratt Formalism
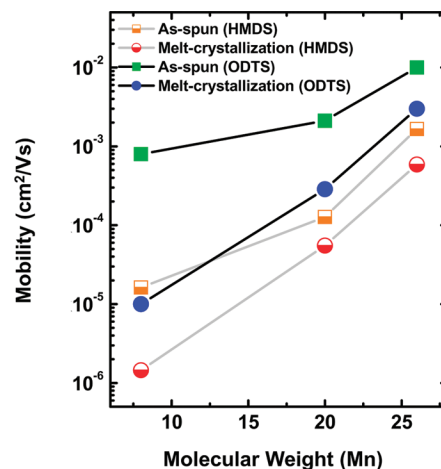
	thickness (nm)		surface roughness (nm)		ρ_e	
	bulk	interface	bulk	interface	bulk	interface
as-spun	110.6	3.2	2.3	0.004	339	287
melt-crystallized	116.0	4.0	5.7	0.6	273	250

features in the experimental data agreed well with curves based on this formalism. The reduction in Kiessig fringes indicates that the roughness of the air/film surface increased from 2.3 to 5.7 nm after melt-crystallization, indicating the formation of well-developed crystallites in the bulk. The roughness of the film/substrate interface also increased from 0.004 to 0.6 nm in the melt-crystallized film. Although the roughness of interface is smaller than that of the bulk, it is critical evidence that the extent of crystallization is enlarged after melt-crystallization of P3HT. In contrast, the electron density at the interfaces is smaller than of the bulk. It means that the growth of crystalline structure at the interfaces does not reach the bulk films. Notably, the electron density of the melt-crystallized film containing well-developed crystallites at the interface is lower than that of the as-spun film at the interface.

To examine in detail the effects of the grain boundaries on μ, we determined the activation energy (E_A) from measurements of the temperature-dependence of the μ. Because charge transport occurs by thermally activated hopping, the number and energy level of the traps can be estimated from E_A. E_A was extracted from the data using the Arrhenius equation: $\mu = \mu_0 \exp(-E_A/kT)$, where k is the Boltzmann constant and T is the absolute temperature. Estimated E_A increased from 81.36 meV before melt-crystallization to 98.71 meV afterward (Figure 6). This result indicates that the formation of grain boundaries in the interfacial channel region enhances the number of trap states, and leads to a reduction in μ.

FIGURE 7. Effects of varying the molecular weight of P3HT on the mobility of as-spun and melt-crystallized P3HT deposited upon ODTS- and HMDS-modified SiO$_2$.
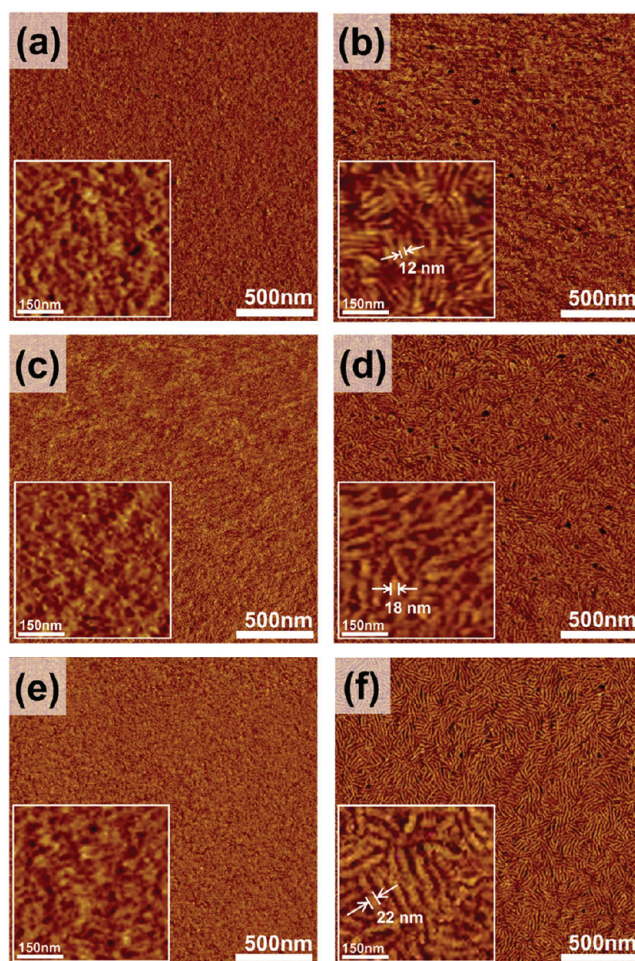
FIGURE 8. AFM phase images (2×2 μm^2) for P3HT with various molecular weights: (a) as-spun P3HT-8 (8 kg/mol), (b) melt-crystallized P3HT-8, (c) as-spun P3HT-20 (20 kg/mol), (d) melt-crystallized P3HT-20, (e) as-spun P3HT-26 (26 kg/mol), (f) melt-crystallized P3HT-26. The scale bar is 500 nm. The insets show AFM phase images at higher magnifications.

FIGURE 6. Temperature dependence of the field-effect mobility of P3HT films. The activation energy (E_A) was determined using the Arrhenius relation: $\mu = \mu_0 \exp(-E_A/kT)$.

We investigated the influence of grain boundaries on μ according to the molecular weight of P3HT (Figure 7). The value of μ increased with the molecular weight of P3HT (24, 25). Although all as-spun P3HT devices had higher μ

than the melt-crystallized devices, the difference between the values of μ increased as the molecular weight of P3HT decreased. Because the crystallinity that results from recrystallization of lower molecular weight P3HT is greater than that of higher-molecular-weight P3HT, P3HT-8 (8 kg/mol) contains more grain boundaries than P3HT-20 (20 kg/mol) and P3HT-26 (26 kg/mol).

AFM phase images were obtained of films of P3HT with various molecular weights (Figure 8). As-spun films show little nanofibrillar crystalline structure. However, high-magnification AFM images reveal the presence of nanofibrillar structures. In contrast, the morphologies of the melt-crystallized P3HT films vary: P3HT-8 contains nanorodlike crystallites, P3HT-26 contains nanowirelike crystallites, and P3HT-20 contains crystallites intermediate between nanorods and nanowires. Obviously, the melt-crystallized P3HT films are more crystalline than the as-spun films. However, the size of crystallites with well-defined grain boundaries decreased as the molecular weight of P3HT decreased: the lateral thickness of P3HT crystallites decreased from 22 nm in 26 kg/mol P3HT film to 12 nm in 8 kg/mol P3HT film. These results indicate that the proportion of grain boundary in the melt-crystallized P3HT films increases as the molecular weight of P3HT decreases, which causes the drastic decrease in μ in melt-crystallized OTFTs.

CONCLUSIONS

The crystallinity and the molecular orientation of P3HT film is improved by melt-crystallization due to $\pi-\pi$ interchain conjugation. However, melt-crystallization reduces μ and results in a transfer curve that is inferior to that of as-spun film. Although nanowirelike crystalline structures are formed as a result of melt-crystallization, well-defined grain boundaries are also formed at the interface, and these may cause the decrease in μ. The temperature-dependent changes in μ indicate that the grain boundaries form traps. The decrease in μ caused by this trapping effect increases as the low-molecular-weight P3HT film decreases. Channel region morphology having enlarged interconnection distance between crystallites appears to explain the cause of decreased μ in melt-crystallized P3HT devices.

Supporting Information Available: Pictures of process of film transfer technique and analysis of X-ray photoelectron spectroscopy (XPS) (PDF). This information is available free of charge via the Internet at http://pubs.acs.org.

REFERENCES AND NOTES

(1) Sirringhaus, H.; Brown, P. J.; Friend, R. H.; Nielsen, M. M.; Bechgaard, K.; Langeveld-Voss, B. M. W.; Spiering, A. J. H.; Janssen, R. A. J.; Meijer, E. W.; Herwig, P.; De Leeuw, D. M. *Nature.* **1999**, *401*, 685–688.
(2) Mcculloch, I.; Heeney, M.; Bailey, C.; Genevicius, K.; Macdonald, I.; Shkunov, M.; Sparrowe, D.; Tierney, S.; Wagner, R.; Zhang, W.; Chabinyc, M. L.; Kline, R. J.; McGehee, M. D.; Toney, M. F. *Nat. Mater.* **2006**, *5*, 328–333.
(3) DeLongchamp, D. M.; Kline, R. J.; Lin, E. K.; Fischer, D. A.; Richter, L. J.; Lucas, L. A.; Heeney, M.; McCulloch, I.; Northrup, J. E. *Adv. Mater.* **2007**, *19*, 833–837.
(4) Horowitz, G.; Hajlaoui, M. E.; Hajlaoui, R. *J. Appl. Phys.* **2000**, *87*, 4456–4463.
(5) Bao, Z.; Dodabalapur, A.; Lovinger, A. J. *Appl. Phys. Lett.* **1996**, *69*, 4108–4110.
(6) Chen, T.-A.; Wu, X.; Rieke, R. D. *J. Am. Chem. Soc.* **1995**, *117*, 233–244.
(7) Marchant, S.; Foot, P. J. S. *Polymer* **1997**, *38*, 1749–1751.
(8) Nakazono, M.; Kawai, T.; Yoshino, K. *Chem. Mater.* **1994**, *6*, 864–870.
(9) Joung, M. J.; Kim, C. A.; Kang, S. Y.; Baek, K.-H.; Kim, G. H.; Ahn, S. D.; You, I. K.; Ahn, J. H.; Suh, K. S. *Synth. Met.* **2005**, *149*, 73–77.
(10) Cho, S.; Lee, K.; Yuen, J.; Wang, G.; Moses, D.; Heeger, A. J.; Surin, M.; Lazzaroni, R. *J. Appl. Phys.* **2006**, *100*, 114503−114503−6.
(11) Mattis, B. A.; Chang, P. C.; Subramanian, V. *Mater. Res. Soc. Symp. Proc.* **2003**, *771*, L10.35.1L10.35.6.
(12) Liu, Y. W.; Oshima, K.; Yamauchi, T.; Shimomura, M.; Miyauchi, S. *Synth. Met.* **1999**, *101*, 451–452.
(13) Lee, Y.; Fukukawa, K.-I.; Bang, J.; Hawker, C. J.; Kim, J. K. *J. Polym. Sci., Part A: Polym. Chem.* **2008**, *46*, 8200–8205.
(14) Lee, B.; Park, Y.-H.; Hwang, Y.-T.; Oh, W.; Yoon, J.; Ree, M. *Nat. Mater.* **2005**, *4*, 147–150.
(15) Lee, B.; Park, I.; Yoon, J.; Park, S.; Kim, J.; Kim, K.-W.; Chang, T.; Ree., M. *Macromolecules.* **2005**, *38*, 4311–4323.
(16) Yoon, J.; Kim, K.-W.; Kim, J.; Heo, K.; Jin, W.; Shin, T. J.; Lee, B.; Pho, Y.; Ahn, B.; Ree, M. *Macromol. Res.* **2008**, *16*, 575–579.
(17) Bolze, J.; Ree, M.; Youn, H. S.; Chu, S.-H.; Char, K. *Langmuir* **2001**, *17*, 6683–6691.
(18) Zhang, R.; Li, B.; Iovu, M. C.; Jeffries-EL, M.; Sauve, G.; Cooper, J.; Jia, S.; Tristram-Nagle, S.; Smilgies, D. M.; Lambeth, D. N.; McCullough, R. D.; Kowalewski, T. *J. Am. Chem. Soc.* **2006**, *128*, 3480–3481.
(19) Kim, Y.; Cook, S.; Tuladhar, S. M.; Choulis, S. A.; Nelson, J.; Durrant, J. R.; Bradley, D. D. C.; Giles, M.; McCulloch, I.; Ha, C.-S.; Ree, M. *Nat. Mater.* **2006**, *3*, 197–203.
(20) Verilhac, J.-M.; LeBlevennec, G.; Djurado, D.; Rieutord, F.; Chouiki, M.; Travers, J.-P.; Pron, A. *Synth. Met.* **2006**, *156*, 815–823.
(21) Grevin, B.; Rannou, P.; Payerne, R.; Pron, A.; Travers, J.-P. *Adv. Mater.* **2003**, *15*, 881–884.
(22) Kline, R. J.; McGehee, M. D.; Toney, M. F. *Nat. Mater.* **2006**, *5*, 222–228.
(23) Cacialli, F.; Wilson, J. S.; Michels, J. J.; Daniel, C.; Silva, C.; Friend, R. H.; Severin, N.; Samori, P.; Rabe, J. P.; O'Connell, M. J.; Taylor, P. N.; Anderson, H. L. *Nat. Mater.* **2002**, *1*, 160–164.
(24) Kline, R. J.; McGehee, M. D.; Kadnikova, E. N.; Liu, J.; Frechet, J. M. J. *Adv. Mater.* **2003**, *15*, 1519–1522.
(25) Kline, R. J.; McGehee, M. D.; Kadnikova, E. N.; Liu, J.; Frechet, J. M. J.; Toney, M. F. *Macromolecules* **2005**, *38*, 3312–3319.
(26) Street, R. A.; Northrup, J. E.; Salleo, A. *Phys. Rev. B* **2005**, *71*, 165202−165202−13.
(27) Kelley, T. W.; Frisbie, C. D. *J. Phys. Chem. B* **2001**, *105*, 4538–4540.

AM9005385